Evaluation of Scale-Adaptive Simulation for Transonic Cavity Flows

Savio V. Babu, George Zografakis, George N. Barakos

CFD Laboratory,
University of Liverpool,
L63 3GH, UK
E-mail: s.babu@liv.ac.uk
E-mail: g.zografakis@liv.ac.uk
E-mail: g.barakos@liv.ac.uk

Alexander Kusyumov

Kazan State Technical University,
10 K. Marx Street, Kazan 420111
Russian Federation, Russia

Abstract: Scale-Adaptive Simulations of flow in clean transonic cavities with and without doors are presented in this paper. Results were also compared with Detached-Eddy Simulations for cavities with length-to-depth ratios of 5 and 7. The Mach and Reynolds numbers (based on the cavity length) were 0.85 and 6.5×10^6 respectively, and the grid sizes were 5.0 million for the clean cavity with doors-off and 5.5 million for the clean cavity with doors-on. Instantaneous Mach number contours showed that the shear layer broke down for both the doors on and doors off cases and that the flows had a high level of unsteadiness inside them. Numerical schlieren contours made it possible to visualise the propagation of pressure waves in and around these cavities. The two L/D ratios of cavities were seen to have similar acoustic signatures reaching maximum sound levels of 170dB. Spectral analyses for the cavities without doors revealed that by changing the length-to-depth ratio from 5 to 7, the dominant acoustic modes at the front and rear of the cavities were shifted from the second and third modes to the first and second modes respectively. Proper Orthogonal Decomposition was used to reduce the data storage using modes constructed from flowfield snapshots taken at regular intervals. Cumulative energy plots of the constructed modes showed that Detached-Eddy Simulations were able to capture 10% more energy for Pressure and Density variables for the same number of modes.

Keywords: aerodynamics; transonic cavity flow; CFD; DES; SAS; POD.

Reference to this paper should be made as follows: Babu, S.V., Zografakis, G., Barakos G.N. and Kusyumov A. (2014) 'Evaluation of Scale-Adaptive Simulation for Transonic Cavity Flows', *International Journal of Engineering Systems Modelling and Simulation*, Vol. x, No. x, pp.xxx–xxx.

Biographical notes: Savio V. Babu graduated with an MEng in Aerospace Engineering from the University of Liverpool and is currently a PhD student at the CFD lab of Liverpool, working on cavity flows. His interest is in transonic cavity flows.

George Zografakis obtained his PhD from the University of Liverpool in 2012 on transition modelling for rotorcraft applications. He is currently a postdoctoral researcher at the University of Liverpool and is interested in turbulence and transition modelling.

George N. Barakos obtained his PhD from UMIST in Manchester, UK, on implicit methods for unsteady turbulent flows. He is the Director of the Augusta Westland Liverpool Advanced Rotorcraft Centre and his interests include rotary wing aerodynamics, wind turbine aerodynamics, cavity flow, turbulence modelling and high performance computing. He teaches several modules on Aerodynamics, Simulation and rotorcraft at undergraduate and postgraduate levels.

Alexander Kusyumov is a professor at the Kazan National Research Technical University in Russia currently working on aerodynamics and aeroacoustics.

This paper is a revised and expanded version of a paper entitled 'Prediction of Acoustics of Transonic Cavities using DES and SAS' presented at the 49th Applied Aerodynamics Symposium of the French Aeronautics and Astronautics Society, Lille, 24th-26th March 2014.

1 Introduction

Unmanned Combat Air Vehicles (UCAVs) are designed for stealth and use cavities for storing weapons. At transonic speeds, the flow inside these cavities become highly unsteady and lead to large acoustic signatures that not only affect the stealth characteristics of the vehicle but also the integrity of its structural components. A similar problem exists with the exposed undercarriage and landing gear bays of aircraft. While wind tunnel and flight test data have been used in the past to study noise generated from landing gears [1, 2, 3, 4], Computational Fluid Dynamics (CFD) is increasingly being used to predict these flows.

Currently, Direct Numerical Simulation (DNS) of transonic cavity flow is not possible, due to the substantial computational resources needed for practical Mach and Reynolds numbers. Studies of cavity flows use CFD based on the use of Reynolds-Averaged Navier-Stokes (RANS) equations together with a turbulence model. Unsteady RANS (URANS), however, is unable to predict the full spectrum of turbulent scales and with Large-Eddy Simulation (LES) being too expensive near wall regions, Detached-Eddy Simulation (DES) is the popular choice for these flows. Store carriage and separation from weapon bays has also received some interest in recent years. Early works have focused on weapon bays idealised as rectangular cavities but the focus is shifting to weapon bays installed in UCAVs and geometrically complex bays. Lawson and Barakos [5] give a detailed account of work relating to UCAVs and transonic cavities.

Simulations of store separation from cavities, for store clearance, are becoming expensive with increasing mesh sizes that account for geometric complexities. This requires faster calculations to allow for numerous simulations under varying conditions. While DES is capable of accurately predicting these flows, it still takes a considerable amount of time on a large number of processors. Since its introduction by Meter *et al.*[6, 7, 8] in 2003, the Scale-Adaptive Simulation (SAS) approach gained popularity due to its LES-like behaviour in highly separated flow regions and found place in several studies. A detailed explanation of the theory and description of the model was given by Menter and Egorov [9] following which Egorov *et al.*[10] presented the application of the SAS model, implemented in ANSYS-FLUENT and ANSYS-CFX, for a range of complex flows. Other than the demonstration of SAS for the M219 cavity case without doors by Egorov *et al.*[10], no other cavity work using SAS is available in open literature. The evaluation of SAS for cavity flows and later for cavities with stores will encourage its use in store separation simulations.

In view of the above, this paper presents results from studies of the SAS approach for cavity flows. The widely used M219 cavity and a cavity of L/D 7 are used for numerical computations with DES, SAS and URANS and the Helicopter Multi-Block (HMB2) flow solver of Liverpool [11]. The M219 clean cavity with and without doors is used here with experimental data obtained from Nightingale *et al.*[12]. Computations were also carried out for the L/D 7 cavity with and without doors, for which experimental and numerical results are lacking. DES based on the Spalart-Allmaras (S-A) turbulence model [13], SAS using the SST turbulence model and URANS using the SST turbulence model were employed for the computations.

Section 1 introduces the motivation behind the current work. Details of the flow solver and the DES and SAS approaches are given in Section 2. Section 2 describes the numerical methods used for post-processing, flow visualisation and data reduction. Grid details and the mesh generation process are explained in Section 4. The results are presented and discussed in Section 5 and a summary with conclusions of the current work is presented in Section 6.

2 FLOW SOLVER

HMB2 is a parallel, cell-centred, finite volume method based flow solver developed at the University of Liverpool and was used for the computations presented in this paper. This section provides information related to the solver and includes the governing equations and a description of the employed turbulence models.

2.1 Governing Equations

HMB2 [11] solves the three-dimensional, unsteady, compressible Navier-Stokes equations on multi-block structured grids. Barakos *et al.*[14] provides a detailed description of multi-block topologies employed in the M219 clean cavity and the 1303 UCAV cavity with a store present. The governing equations are the unsteady three-dimensional compressible Navier-Stokes equations, written in dimensionless form as:

$$\frac{\partial Q}{\partial t} + \frac{\partial}{\partial x}\left(F^i + \frac{1}{Re}F^v\right) + \frac{\partial}{\partial y}\left(G^i + \frac{1}{Re}G^v\right) + \frac{\partial}{\partial z}\left(H^i + \frac{1}{Re}H^v\right) = 0 \quad (1)$$

where Q contains the unsteady terms and F, G and H are spatial flux vectors, split into their inviscid (i) and viscous (v) parts. The code solves the governing equations on multi-block structured grids using a cell-centred finite volume method. The convective terms are discretised using either Osher's [15] or Roe's [16] scheme. Monotone Upwind Schemes for Scalar Conservation Laws (MUSCL) interpolation [17] is used to provide formally third order accuracy and the Van Albada limiter [18] is used to avoid spurious oscillations across shocks. An implicit, dual step method [19] is used for time-marching and the final algebraic system of

equations is solved using a Conjugate Gradient method, in conjunction with Block Incomplete Lower-Upper (BILU) factorisation [20]. A number of turbulence models including one and two-equation statistical models as well as Large-Eddy Simulation and Detached-Eddy Simulation have been implemented into the code. More details of the employed CFD solver and turbulence models are given in Barakos *et al.*[14]. For the work presented in this paper, DES was employed along with the Spalart-Allmaras turbulence model [13] and SAS and URANS utilised the Shear Stress Transport (SST) model [21].

2.2 Detached-Eddy Simulation

Despite the potential of LES, there are problems in resolving the near-wall turbulent stresses since the required resources approach those of Direct Numerical Simulation. Pure LES gives about 10 times higher Reynolds numbers than DNS but is of limited application for the flow at hand. While RANS is an option, another alternative that has gained popularity over the years involves hybrids of LES and RANS such as DES. The original idea of DES was postulated by Spalart and Allmaras [13]. Its underlying principle involved using RANS for the near-wall and boundary layer and LES everywhere outside. Spalart modified the S-A model to achieve a DES equivalent. The wall distance (d) is now recomputed according to the DES principle and represented by $\tilde{d}$. In the pure one-equation S-A turbulence model, the terms $\tilde{d}$ and d are identical. However, the DES formulation of $\tilde{d}$ is given by:

$$\tilde{d} = C_{DES}\Delta \tag{2}$$

where C_{DES} is a constant and Δ is the metric of the grid size. In practice, the distance to the wall in the DES formulation of the one-equation S-A model is expressed as a comparison between the actual distance to the wall and that calculated by $C_{DES}\Delta$, which essentially computes the size of the maximum cell length:

$$\tilde{d} = \min\left(d, C_{DES}\Delta\right) \tag{3}$$

$$\Delta = \max\left(\Delta_x, \Delta_y, \Delta_z\right) \quad \forall \quad \text{cell.} \tag{4}$$

When the cell length ($C_{DES}\Delta$) is less than the actual distance to the nearest wall (d), LES is triggered. RANS is activated when the converse occurs. This boundary between LES and RANS is therefore completely dependent on the geometry and on the density of the computational mesh. Note that other metric relations are also possible.

2.3 Scale-Adaptive Simulation

The governing equations of the SST-SAS model differ from those of the SST-RANS model by an additional source term (Q_{SAS}) in the transport equation for the turbulence eddy frequency ω:

$$\frac{\partial(\rho k)}{\partial t} + \frac{\partial \rho u_j k}{\partial x_j} = P_k - \rho c_\mu k\omega + \frac{\partial}{\partial x_j}\left[\left(\mu + \frac{\mu_t}{\sigma_k}\right)\frac{\partial k}{\partial x_j}\right] \tag{5}$$

$$\frac{\partial(\rho\omega)}{\partial t} + \frac{\partial \rho u_j \omega}{\partial x_j} = \alpha\frac{\omega}{k}P_k - \rho\beta\omega^2 + Q_{SAS} + \frac{\partial}{\partial x_j}\left[\left(\mu + \frac{\mu_t}{\sigma_\omega}\right)\frac{\partial \omega}{\partial x_j}\right] + (1-F_1)\frac{2\rho}{\sigma_{\omega 2}}\frac{1}{\omega}\frac{\partial k}{\partial x_j}\frac{\partial \omega}{\partial x_j} \tag{6}$$

The additional source term Q_{SAS} is given by:

$$Q_{SAS} = max\left[\rho\zeta_2\kappa S^2\left(\frac{L}{L_{vK}}\right)^2 - C\frac{2\rho k}{\sigma_\Phi}max\left(\frac{1}{\omega}\frac{\partial\omega}{\partial x_j}\frac{\partial\omega}{\partial x_j}, \frac{1}{k}\frac{\partial k}{\partial x_j}\frac{\partial k}{\partial x_j}\right), 0\right] \tag{7}$$

where ζ_2=3.51, σ_Φ=2/3 and C=2.

The length scale of the modelled turbulence L, and the von Karman length scale L_{vK} are defined as:

$$L = \frac{\sqrt{k}}{c_\mu^{1/4}\omega}, \quad L_{vK} = \frac{\kappa S}{|U''|} \tag{8}$$

where $\kappa = 0.41$ is the von Karman constant.

The first velocity derivative $U''(y)$ is represented in L_{vK} by S, which is a scalar invariant of the strain rate tensor S_{ij}:

$$S = \sqrt{2S_{ij}S_{ij}}, \quad S_{ij} = \frac{1}{2}\left[\frac{\partial U_i}{\partial x_j} + \frac{\partial U_j}{\partial x_i}\right] \tag{9}$$

The same S is used also in the production term $P_k = \mu_t S^2$. The second velocity derivative $U''(y)$ is generalised to 3D using the magnitude of the velocity Laplacian:

$$|U''| = \sqrt{\sum_{(i)}\left(\frac{\partial^2 U_i}{\partial x_j \partial x_j}\right)^2} \tag{10}$$

In order to provide proper damping of resolved turbulence at high wave numbers, the SST-SAS model requires a lower constrain on the L_{vK} given by:

$$L_{vK} = max\left(\frac{\kappa S}{|U''|}, C_s\sqrt{\frac{\kappa\zeta_2}{(\frac{\beta}{c_\mu}) - \alpha}}\cdot\Delta\right) \tag{11}$$

The limiter is proportional to the grid cell size Δ, which is calculated as the cubic root of the control volume size:

$$\Delta = \Omega_{CV}^{1/3} \tag{12}$$

The purpose of this limiter is to control damping of the finest resolved turbulent fluctuations. The structure of the limiter is derived from analysing the equilibrium eddy viscosity of the SST-SAS model [9]. Assuming a balance between the production and destruction of the kinetic energy of turbulence in both transport equations, the following relation between the equilibrium eddy viscosity are derived:

$$\mu_t^{eq} = \rho \left(\sqrt{\frac{(\frac{\beta}{c_\mu}) - \alpha}{\kappa \zeta_2}} L_{vK} \right)^2 S \tag{13}$$

which has similar structure as the subgrid scale eddy viscosity in the LES model

$$\mu_t^{LES} = \rho (C_S \Delta)^2 S \tag{14}$$

The limiter, imposed on the L_{vK} value, must prevent the SAS eddy viscosity from decreasing below the LES subgrid-scale eddy viscosity:

$$\mu_t = max(\mu_t^{SAS}, \mu_t^{LES}) \tag{15}$$

3 NUMERICAL METHODS

This section presents the analysis techniques carried out on the unsteady data, the methods of flow visualisation, and reduction of the generated flow data.

3.1 Post-Processing Methods

The CFD solver outputs flow-field files written at specific instances of time as specified by the user. In addition to this it also outputs data from specific 'probes that are placed in the flow. The locations of the probes are defined at the beginning of the computation and are then written at every time step performed. For the cavity flow computations, probes are usually defined at the same locations as the Kulite^{TM} pressure transducers in experiments and are therefore sampled at a high enough frequency for spectral analyses.

The Power Spectral Density (PSD), Overall Sound-Pressure Level (OASPL) and Band-Integrated Sound-Pressure Level (BISPL) are used to compare numerical and experimental unsteady pressure data along the cavity floor. The PSD is used to study the frequency content of a signal at a given location and is based upon the unsteady pressure p', where $p' = p - \overline{p}$. The PSD was calculated using the Burg Estimator [22] (also known as Maximum Entropy Methods or MEM) as it produces better resolved peaks for short signals than traditional Fast Fourier Transforms (FFT) [23] For a description of the PSD in terms of decibels (dB), the natural definition is that of the Sound-Pressure spectrum Level (SPL) [24]:

$$SPL(f) = 10 \ \mathrm{LOG}_{10} \left[\frac{PSD(f) \ \Delta f_{ref}}{p_{ref}^2} \right] \tag{16}$$

where Δf_{ref} is a reference frequency, usually set to 1 Hz and p_{ref} is the international standard for the minimum audible sound, which has the value of 2×10^{-5} Pa [24].

The variation in pressure levels along the cavity floor was studied using the Root-Mean-Square (RMS) of the unsteady pressure, p'_{rms}, and can be obtained from the measurements using the following equation:

$$p'_{rms} = \sqrt{\frac{1}{N} \sum (p')^2} \tag{17}$$

Although p'_{rms} is measured in Pascals (or any other unit of pressure), it is customary in cavity flow studies to report it as the Overall Sound-Pressure Level(OASPL) [24]:

$$OASPL = 20 \ \mathrm{LOG}_{10} \left[\frac{p'_{rms}}{p_{ref}} \right] \tag{18}$$

which has the units of decibels. BISPL plots show the energy content within a particular frequency range and is calculated using the following equation:

$$BISPL = 20 \ \mathrm{LOG}_{10} \left[\left(\int_{f_1}^{f_2} PSD(f) \right)^{1/2} \cdot \frac{1}{p_{ref}} \right] \tag{19}$$

where f_1 and f_2 are the lower and upper limits of the desired frequency range. Although the magnitude of the BISPL aids in identifying which frequencies are significant, the shape of each banded mode is also important as it represents how each frequency band varies along the cavity length. For cavity flow studies, the BISPL plots are usually centred around the first four Rossiter Modes.

Comparison of numerical and experimental data for unsteady flows is not simple. For cavity flows in particular, a mode switching phenomenon occurs. Therefore in processing, the experimental data is split into segments equalling the length of the numerical signal, with each segment having a 90% overlap. Each segment is then processed using the methods given above and at each location the maximum and minimum levels in the OASPL and BISPL are recorded. The curve plotted in the PSD is the segment deemed to be the 'best fit' to the numerical data, where the metric used to define the best fit was the OASPL.

The tones in the PSD are usually termed Rossiter modes [25] and a semi-empirical formula is available for the estimation of their frequencies. Rossiter, based the formula on experimental results over a range of Mach numbers from 0.4 to 1.4 and on various cavity aspect ratios. However, outside this range the accuracy of the predictions decreases and so Heller [26] modified the original formula to compensate. The modified version is as follows:

$$f_m = \frac{U_\infty}{L} \left[\frac{m - \alpha}{M_\infty \left(1 + \left(\frac{\gamma - 1}{2}\right) M_\infty^2\right)^{-1/2} + 1/\kappa_\nu} \right] \tag{20}$$

where f_m is the frequency of mode m, U_∞ and M_∞ is the free-stream velocity and Mach number respectively and L is the cavity length. γ is the ratio of specific

heats, α represents a phase shift and κ_ν is a constant dependant on the cavity geometry and test conditions. These constants have the values 1.4, 0.25 and 0.57 respectively. The formula is used here for comparisons with CFD results.

3.2 Flow-Field Analysis

3.2.1 Q-Criteria

Turbulent structures are inherently three-dimensional and so to better identify them within the flow, the Q-Criteria is used. Hunt [27] proposed the Q-Criteria to identify vortex cores and reflects the amount of strain and vorticity in a vector field. Let ∇u denote the gradient of the velocity field. The Q-Criteria is then defined as the positive second invariant of the velocity gradient tensor:

$$\begin{aligned} Q &\equiv \frac{1}{2}\left(u_{i,i}^2 - u_{i,j}u_{j,i}\right) \\ &= -\frac{1}{2}\left(u_{i,j}u_{j,i}\right) \\ &= \frac{1}{2}\left(\| \mathbf{\Omega} \|^2 - \| \mathbf{S} \|^2\right) \end{aligned} \tag{21}$$

where $\mathbf{S}$ and $\mathbf{\Omega}$ are the symmetric and anti-symmetric components of ∇u. The strain tensor is defined as the symmetric part, and the antisymmetric part is closely related to the vorticity. Thus, the Q-Criteria represents the local balance between shear strain rate and vorticity magnitude [28]. Where $Q > 0$, vorticity dominates strain and so identifies a vortex region.

3.2.2 Numerical Schlieren

In order to visualise the unsteadiness in the flow-field, instantaneous numerical schlieren is calculated. The numerical schlieren variable requires the calculation of the density gradient magnitude (DG) and is defined as:

$$NS = c_1 \exp\left[\frac{-c_2(DG - DG_{min})}{(DG_{max} - DG_{min})}\right] \tag{22}$$

where c_1 and c_2 are constants with values of 0.8 and 10.0 respectively.

3.3 Proper Orthogonal Decomposition

The Proper Orthogonal Decomposition (POD) is a technique used in image processing, signal analysis and data compression [29]. It aims to obtain low-dimensional approximations of high-dimensional processes, therefore eliminating information which has little impact on the overall process. It was first introduced in the context of fluid mechanics and turbulence by Lumley [30] to decompose the flow into modes. These modes identify the large coherent structures which contribute to the flow.

The principle behind POD is that any function can be written as a linear combination of a finite set of functions, termed basis functions. Any set of functions or vectors, f_1, f_2, ..., f_n are linearly independent if they satisfy the following equation:

$$\alpha_1 f_1 + \alpha_2 f_2 + ... + \alpha_n f_n \neq 0 \tag{23}$$

where the coefficients α_1, α_2,..., α_n are constants and non-zero. If a vector space V, can be described by a subset of vectors v_1, v_2, ...,v_n, then these form a basis set if they are linearly independent and they can be written in a linear combination of the form:

$$V = \alpha_1 v_1 + \alpha_2 v_2 + ... + \alpha_n v_n \tag{24}$$

The set of basis vectors can also be an orthonormal basis set if the inner product of v_i and v_j is zero, where $i \neq j$. Also, they are required to have a length of 1 (i.e. the inner product of v_i and v_i is 1).

Three different methods fall under the generalised term of Proper Orthogonal Decomposition: Karhunen-Loeve Decomposition (KLD), Principal Component Analysis (PCA) and Singular Value Decomposition (SVD). However, in the context of turbulence and fluid mechanics, if the acronym POD is used, it generally means KLD.

4 MODEL GEOMETRY AND MESH GENERATION

In this section, the mesh generation process applied in this work is discussed. For all configurations, the geometry, the structured multi-block topologies and the mesh were generated using ICEMCFD v13 [31]. The following sections discuss the grids for the M219 cavity configurations.

Experimental pressure measurements were obtained at Bedford, UK [32]. Clean cavities were studied with and without doors. The doors prevented any leakage at the cavity edges in the spanwise direction forcing the flow to channel into the cavity.

The L/D 5 cavity model (with width-to-depth ratio of 1) measured 20 in. in length and 4 in. in width and depth. The generic cavity rig model (Fig. 1) was positioned at zero incidence and sideslip and the wind tunnel was operated at a Mach number of 0.85 and atmospheric pressure and temperature. The Reynolds numbers (based on the cavity length) was 6.78 million for the clean cavity with and without doors. Unsteady pressure measurements were taken inside the cavity via 10 pressure transducers, shown in Fig. 2, on the cavity floor, aligned along the rig center [32, 12]. The data was sampled at a rate of 6 kHz for approximately 3.5s.

The flow domain used for computations is shown in Fig. 3, along with the applied boundary conditions. The cavity was modelled on the experimental setup, with all solid surfaces having no-slip boundary conditions. The values at the far-field were extrapolated, and so the far-field boundaries had to be set a large distance away from the cavity. Therefore, the domain extended five cavity lengths above the surface of the plate and an extra

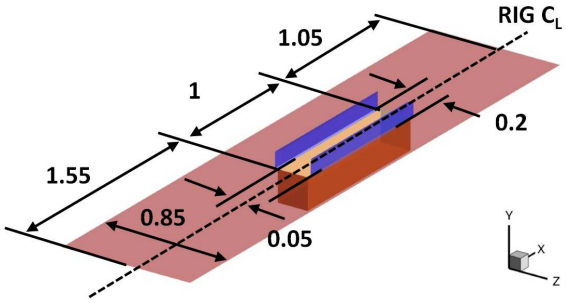

Figure 1: Schematic of the model geometry for the clean cavity with doors L/D 5.

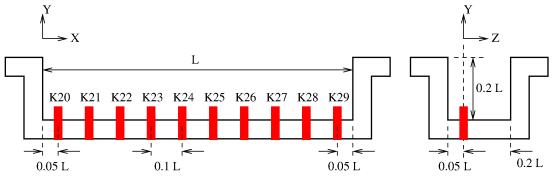

(a) Y-X view (b) Y-Z view

Figure 2: Locations of the Kulites^{TM} sensors used in combination with the M219 cavity.

two cavity lengths around the plate on each side. The boundary conditions for extra section around the plate were set to Y-symmetry, which imposed a slip condition so that no boundary layer would build up.

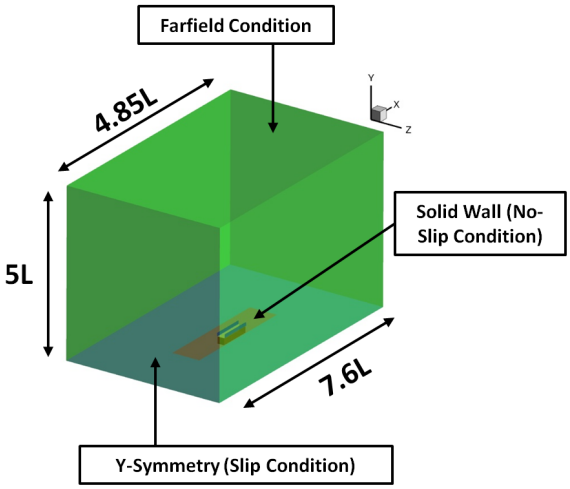

Figure 3: Schematics of the computational domain for the clean cavity with doors L/D 5.

The geometry used to create the grids was based on the wind-tunnel experiments. A schematic is shown in Fig.1. CFD grids of approximately 5.0 million cells (doors-off) and 5.5 million (doors-on) were used to perform computations for the clean cavity, where the grid densities were based on previous experience with the numerical method[14].

For all computed cases, the free-stream Mach number was kept at 0.85 and the Reynolds number based on the length of the cavity was 6.5×10^6 (based on the cavity length). Past work [14] has shown that reducing the Reynolds number to one million had little effect on the cavity flow-field. The recent results were kept at this Reynolds number, so that they could be compared to the experimental data. Details of the computations and the associated grids used in this work are given in Table 1.

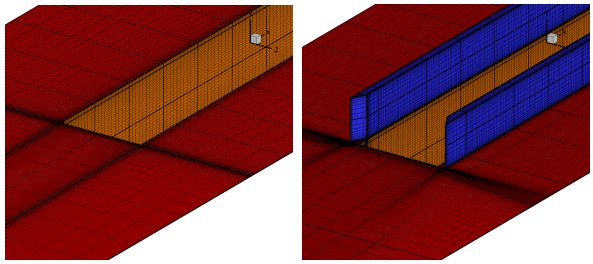

(a) Clean cavity without doors (b) Clean cavity with doors

Figure 4: Surface mesh for the clean cavity L/D 5 without doors (a) and with doors (b).

Table 1 Summary of computational mesh details.

Computation	Method	Grid Size (10^6)	CFD Time -Step (10^{-5}s)
CC, L/D 5, Doors off	DES S-A	5.0	2.19
	SAS SST	5.0	17.58
CC, L/D 5, Doors on	DES S-A	5.5	2.19
	SAS SST	5.5	17.58
CC, L/D 7, Doors off	DES S-A	7.0	2.19
	SAS SST	7.0	17.58
CC, L/D 7, Doors on	DES S-A	7.5	2.19
	SAS SST	7.5	17.58

CC: Clean Cavity, $S-A$: Spalart Allmaras, Mach number: 0.85 and Reynolds number: 6.0×10^6 (based on the cavity length).

5 Results And Discussion

5.1 Instantaneous Flow-Field

Instantaneous contours of Mach number for the clean cavities without doors for L/D of 5 and 7 are shown in Figs. 5(a) and 5(c), respectively, using SAS with one slice in each direction to have a three-dimensional view inside the cavity. The unsteadiness and breakdown of the shear layer is seen as it separates from the leading edge of the cavity at about a third of its length. For both cavities, L/D 5 and 7, the doors-off case showed 'spillages' over the edges of the cavity. The doors on cases, however, caused the early breakdown of the shear layer and restricted the flow along the spanwise direction (Fig. 5(b) and 5(d)).

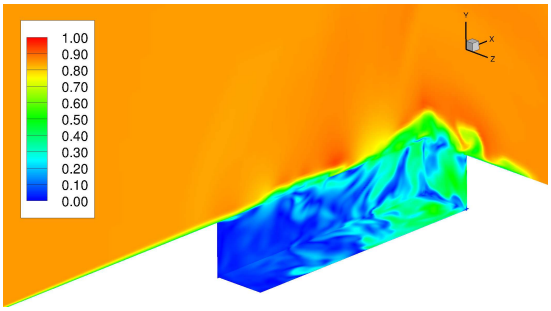

(a) Clean cavity, L/D 5, doors off

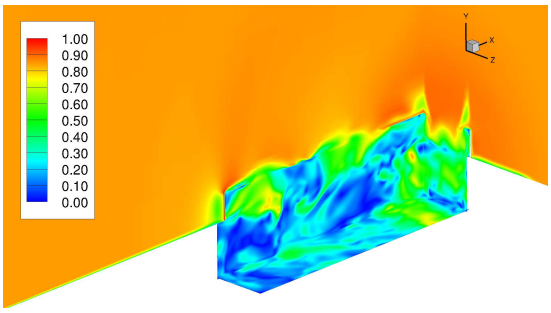

(b) Clean cavity, L/D 5, doors on

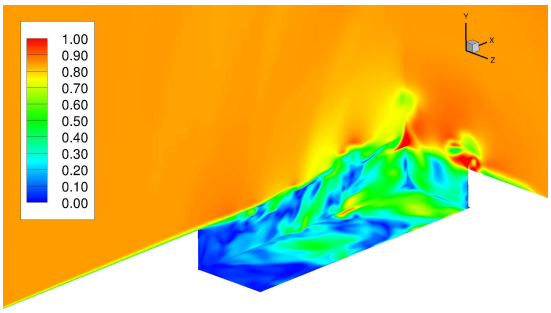

(c) Clean cavity, L/D 7, doors off

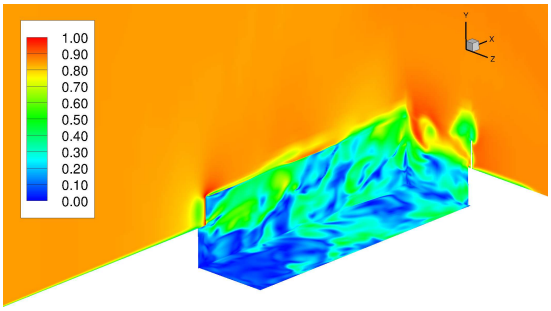

(d) Clean cavity, L/D 7, doors on

Figure 5: Instantaneous contours of Mach number for the clean cavity with L/D 5 (a,b) and L/D 7 (c,d) as predicted using SAS. Planes are located at x/L=0.99, y/L=-0.19 and z/L=-0.04.

(a) Clean cavity, L/D 5, doors off

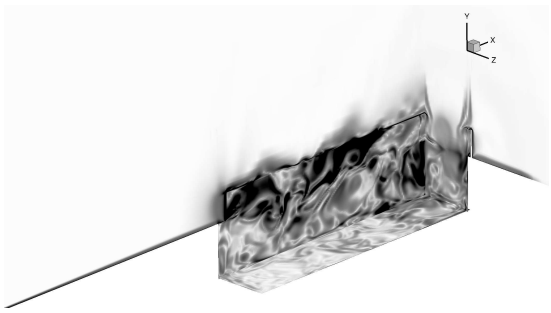

(b) Clean cavity, L/D 5, doors on

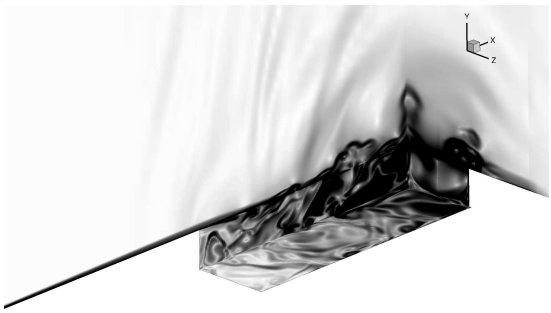

(c) Clean cavity, L/D 7, doors off

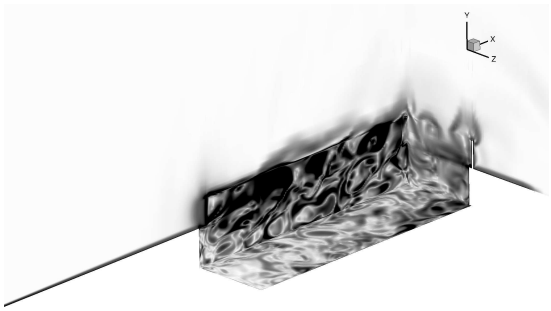

(d) Clean cavity, L/D 7, doors on

Figure 6: Instantaneous contours of Numerical schlieren for the clean cavity with L/D 5 (a,b) and L/D 7 (c,d) as predicted using SAS. Planes are located at x/L=0.99, y/L=-0.19 and z/L=-0.04.

The propagation of pressure waves out of the cavity is visualised using numerical schlieren contours for all L/D configurations with and without doors and is shown in Fig. 6 along three directions. Strong acoustic waves are observed for the clean cavity case without doors. Structures in the shear layer travel toward the aft wall while outside the cavity and reflected acoustic waves travel out and toward the front wall.

Contours of Q-Criteria (Fig. 7) show that the flow for the clean cavities without doors contained large structures that existed for almost the whole cavity length with structures spilling over the side walls. The channelling effect of the doors restricted the flow and the structures for these cases.

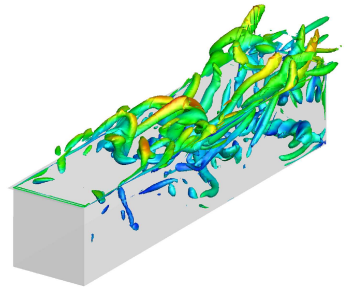

(a) Clean cavity, L/D 5, doors off

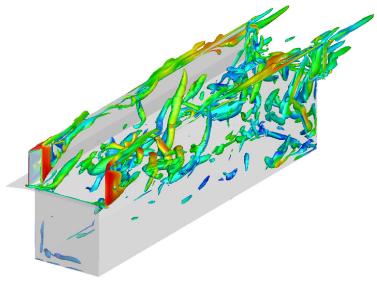

(b) Clean cavity, L/D 5, doors on

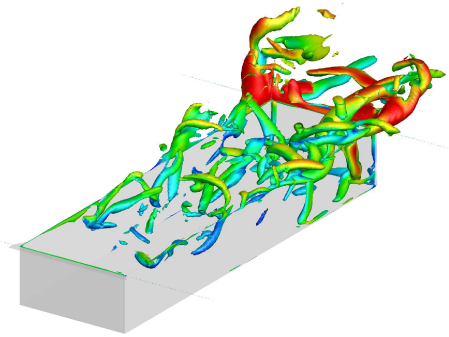

(c) Clean cavity, L/D 7, doors off

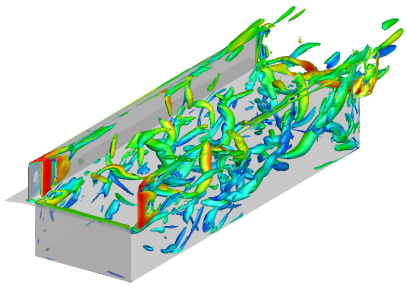

(d) Clean cavity, L/D 7, doors on

Figure 7: Instantaneous iso-surfaces of Q-Criteria for the clean cavity with L/D 5 (a,b) and L/D 7 (c,d) as predicted using SAS. Iso-surfaces at Q=2000 are shown and coloured with Mach number ranging between 0.0 (blue) and 1.0 (red).

5.2 Spectral Analysis for Doors Off Computations

Power Spectral Density (PSD) plots of pressure for the doors off cases for L/D 5 and L/D 7 cavities are shown in Figs. 8 and 9, respectively, comparing DES, SAS and URANS methods with experimental data for the M219 cavity. The results are also compared against modes obtained from Rossiter's equation [25]. The plots correspond to three pressure probe locations on the cavity floor at $x/L = 0.05$, $y/L = 0.50$ and $z/L = 0.90$ respectively that coincide with the locations of the Kulites^{TM} in the M219 cavity.

Comparisons for the L/D 5 cavity in Fig 8 showed that SAS and DES compare well with experimental results while URANS does not correctly predict tones at the first two Kulite locations. The two dominant acoustic modes (modes two and three) at the front (Fig 8(a)) and aft (Fig 8(c)) of the cavity are predicted by DES and SAS as well as the dominant second mode in the middle of the cavity (Fig 8(b)). Towards the leading edge, URANS does not compare well and begins to capture spurious tones at the middle and aft of the cavity. Similar comparisons for the L/D 7 cavity in Fig 9 showed that SAS results compare well with DES results while URANS shows considerable differences. The two dominant acoustic modes (modes one and two) at the front (Fig 9(a)) and aft (Fig 9(c)) of the cavity are predicted by DES and SAS as well as the dominant second mode in the middle of the cavity (Fig 9(b)).

Increasing the L/D from 5 to 7 caused a shift in the dominant tones that were excited inside the cavity. At the front and aft regions this was a shift from modes two and three to modes one and two going from L/D 5 to L/D 7. Both cavities had these modes dominating the middle of the cavity with the L/D 7 being 10dB lower then the L/D 5.

OASPL plots for the doors off cases for L/D 5 and L/D 7 cavities are shown in Fig. 10 comparing DES, SAS and URANS methods. For the L/D 5 cavity, experimental data for the M219 cavity was also included. The plots correspond to ten pressure probe locations along the length of the cavity on the cavity floor that coincide with the locations of the Kulites^{TM} in the M219 cavity. DES and SAS results for the L/D 5 cavity show good comparison with the experimental data with an almost constant overprediction of 5dB along the length of the cavity. Both methods captured the shape of the experimental data. The URANS predicted a similar shape to the experimental data but with an almost constant underprediction of 5dB along the length of the cavity. Results for the L/D 7 cavity show that SAS, DES and URANS have similar trends in terms of the shape of the curve and magnitude at each probe location.

The BISPL plots for the L/D 5 cavity in Fig. 11 showed that the first three modes are predicted well by both DES and SAS. All three methods (DES, SAS and URANS) captured the overall shapes of the first four modes with the differences arising mainly in the magnitude being overpredicted (DES/SAS) or

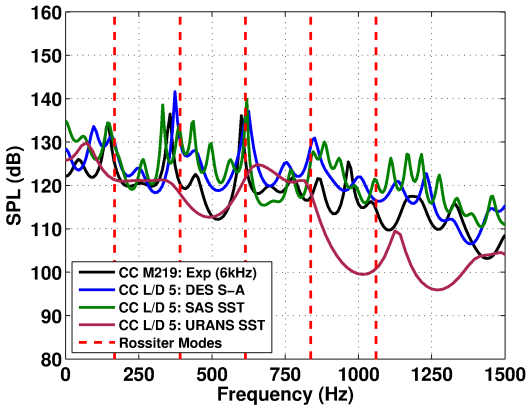

(a) $x/L = 0.05$

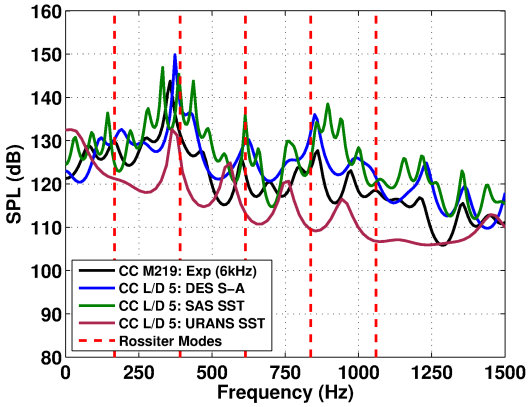

(b) $x/L = 0.50$

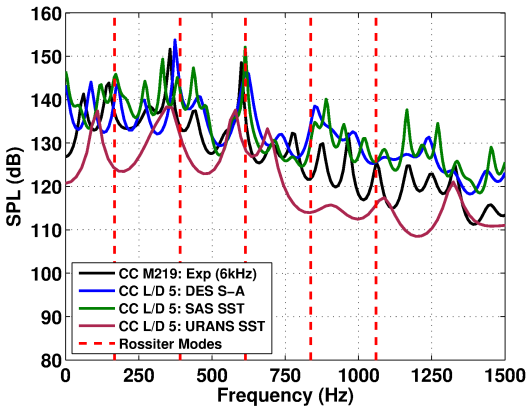

(c) $x/L = 0.95$

Figure 8: PSD plots for the clean cavity L/D 5 comparing results from DES, SAS and URANS methods to experimental data for the M219 cavity from Nightingale et al[12]. Plots are for the front (a), middle (b) and rear (c) transducers on the cavity floor and presented in terms of SPL. CC - Clean Cavity, S-A - Spalart Allmaras.

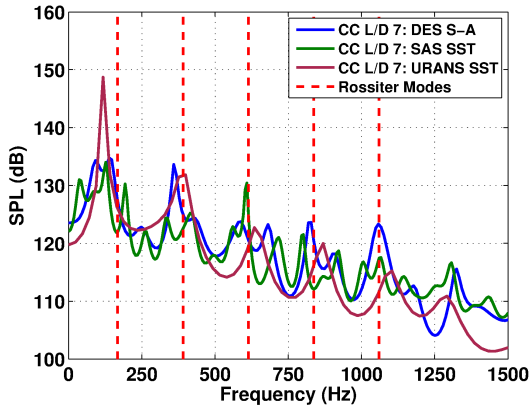

(a) $x/L = 0.05$

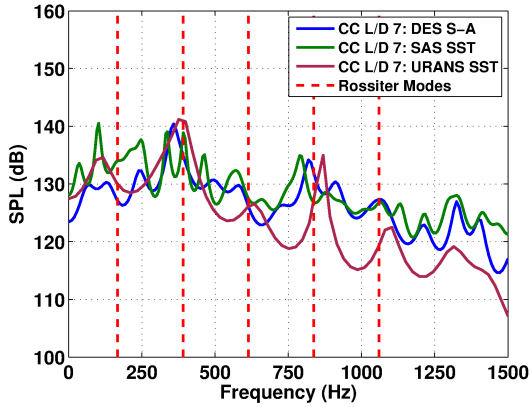

(b) $x/L = 0.50$

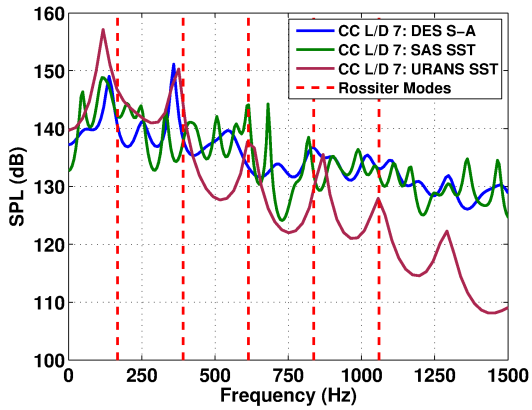

(c) $x/L = 0.95$

Figure 9: PSD plots for the clean cavity L/D 7 comparing results from DES, SAS and URANS methods. Plots are for the front (a), middle (b) and rear (c) transducers on the cavity floor and presented in terms of SPL. CC - Clean Cavity, S-A - Spalart Allmaras.

underpredicted (URANS). For all modes, DES and SAS have similar shapes and magnitudes and overpredict the experimental data by about 4dB . URANS on the other hand, managed to predict the shapes of the first three modes but failed with the higher frequency mode. The shapes of the curves are reasonably predicted given the relatively coarse mesh explored here, and based on experience with finer grids[14], the results are seen as satisfactory for DES/SAS comparisons.

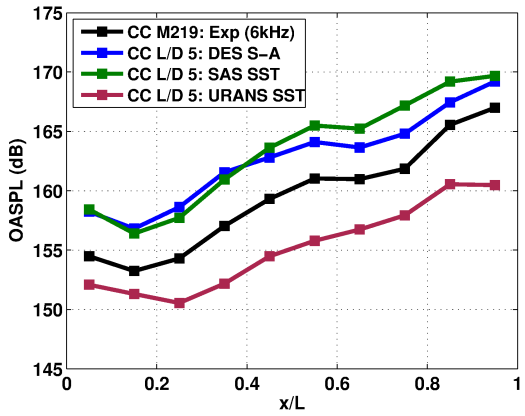

(a) Clean Cavity L/D 5

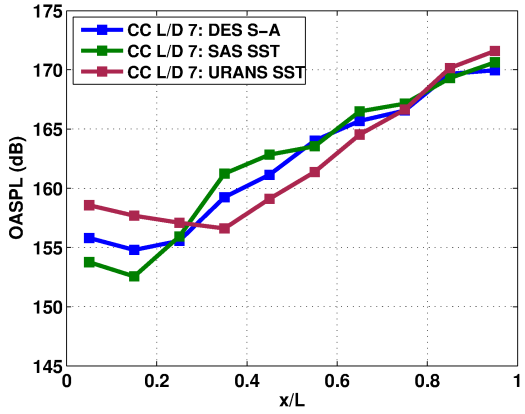

(b) Clean Cavity L/D 7

Figure 10: OASPL along the cavity floor for the clean cavity L/D 5 and 7. For the L/D 5 cavity, plots are also compared to experimental data from Nightingale *et al.*[12].

Unlike the L/D 5 cavity, URANS showed better comparisons for the L/D 7 cavity (Fig. 12). Not only did URANS capture the shapes of the modes quite well, it did so with similar magnitudes to that of DES and SAS, differing only from the middle to the rear of the cavity where the flow completely broke down. DES and SAS show very similar results to each other across the board. Overall the shapes of the BISPL curves look similar between the L/D 5 and L/D 7 cavity except for mode two where the 'W' shape is more pronounced in the L/D 5 cavity.

5.3 Spectral Analysis for Doors On Computations

PSD plots of pressure for the doors on cases for L/D 5 and L/D 7 cavities are shown in Figs. 13 and 14, respectively, comparing DES, SAS and URANS methods with experimental data for the M219 cavity with doors on. DES and SAS showed similar results between each other and good agreement with the experiment for the L/D 5 cavity (Fig 13). Low energy high frequency modes were also captured by DES and SAS. Similar

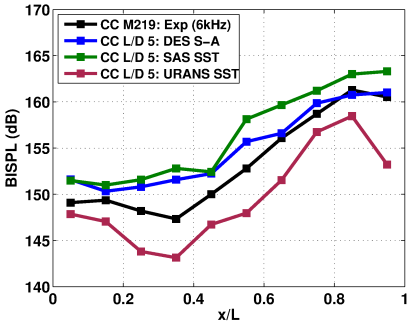

(a) Mode 1: $50 \leq f \leq 250$ Hz

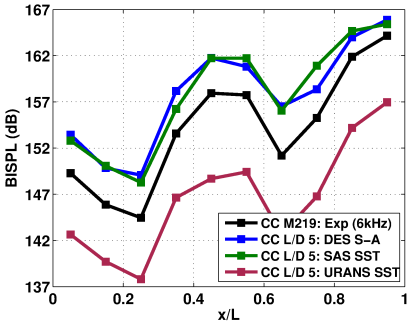

(b) Mode 2: $250 \leq f \leq 450$ Hz

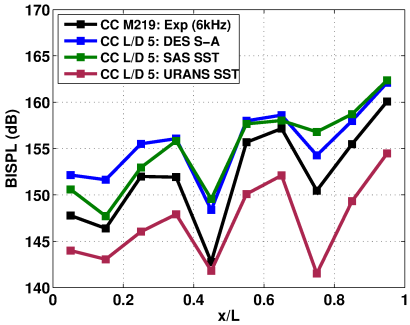

(c) Mode 3: $500 \leq f \leq 700$ Hz

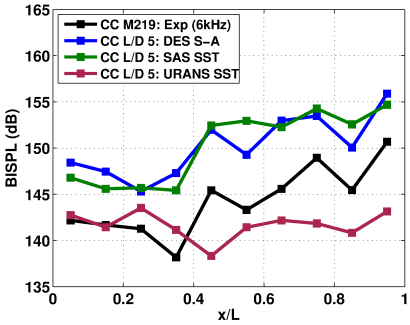

(d) Mode 4: $700 \leq f \leq 900$ Hz

Figure 11: BISPL along the cavity floor for the clean cavity L/D 5. Plots compare results from DES, SAS and URANS methods to experimental data from Nightingale *et al.*[12].

comparisons for the L/D 7 cavity in Fig 14 showed that SAS results compared well with DES, with both methods capturing the dominant second mode across

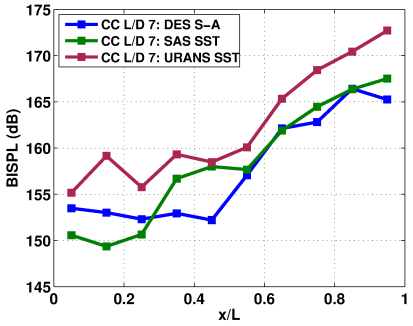

(a) Mode 1: $50 \leq f \leq 250$ Hz

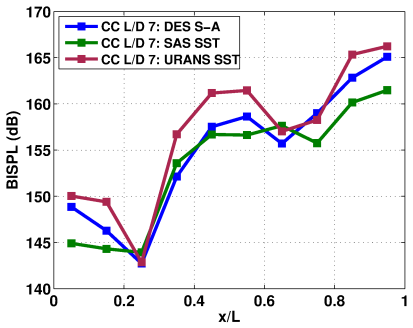

(b) Mode 2: $250 \leq f \leq 450$ Hz

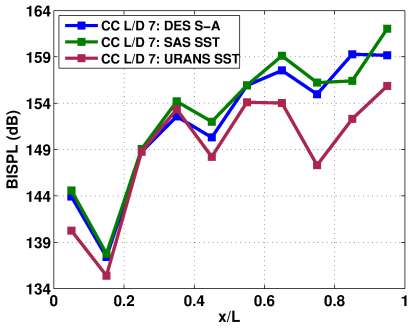

(c) Mode 3: $500 \leq f \leq 700$ Hz

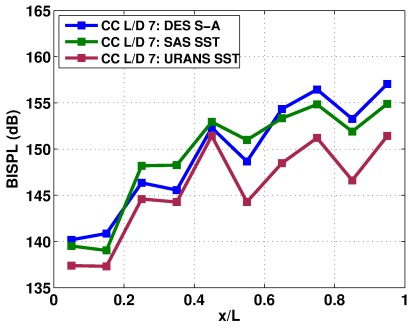

(d) Mode 4: $700 \leq f \leq 900$ Hz

Figure 12: BISPL along the cavity floor for the clean cavity L/D 7. Plots compare results from DES, SAS and URANS methods.

the length of the cavity. In both cases, URANS did not give a good prediction compared to DES and SAS. The addition of the doors did not cause a shift in the dominant frequencies between the L/D 5 and L/D 7 unlike the case with doors off. However, like before the L/D 7 had a reduction of about 10dB at the second mode. The addition of the doors is seen to channel and constrain the oscillation of the flow in both cases.

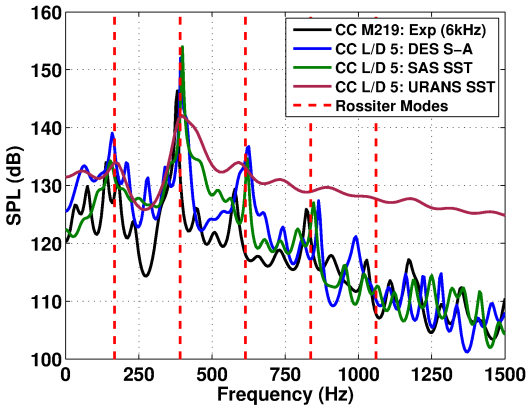

(a) $x/L = 0.05$

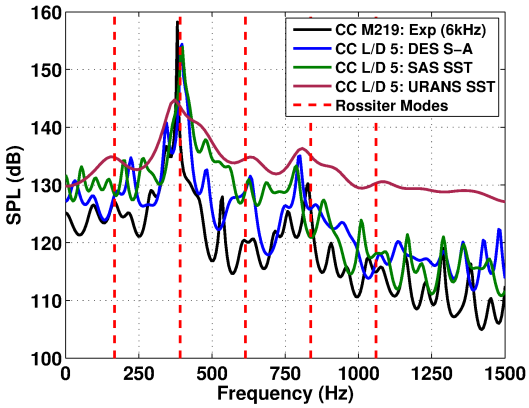

(b) $x/L = 0.50$

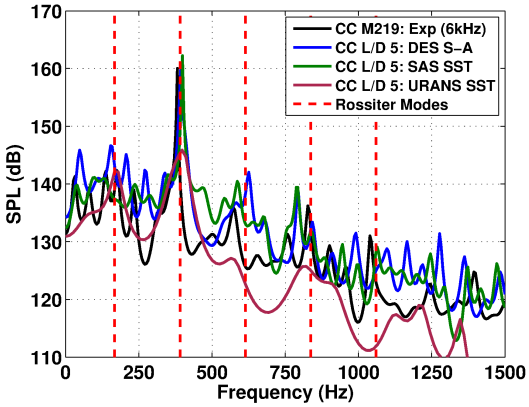

(c) $x/L = 0.95$

Figure 13: PSD plots for the clean cavity L/D 5 with doors comparing results from DES and SAS methods to experimental data for the M219 cavity from Nightingale et al[12]. Plots are for the front (a), middle (b) and rear (c) transducers on the cavity floor and presented in terms of SPL. CC - Clean Cavity, S-A - Spalart Allmaras.

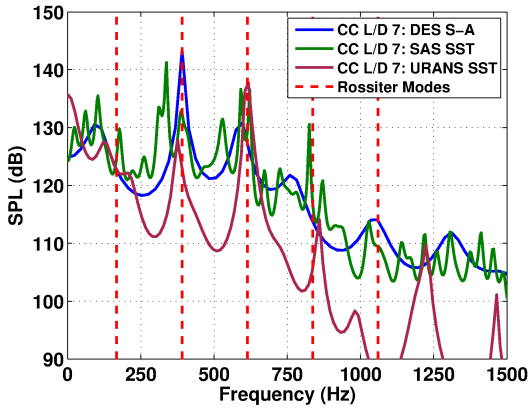

(a) $x/L = 0.05$

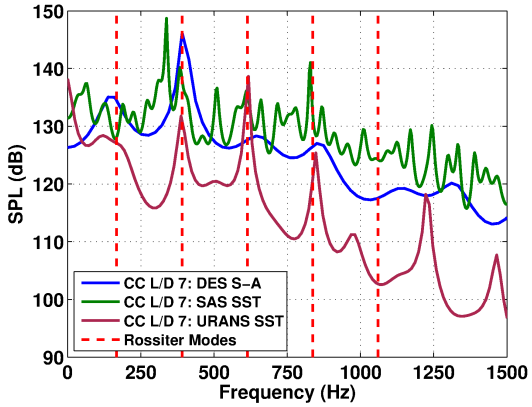

(b) $x/L = 0.50$

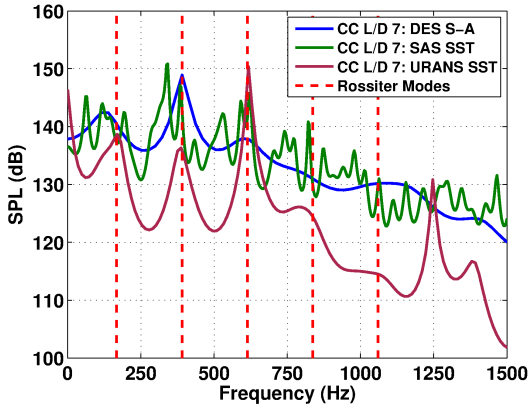

(c) $x/L = 0.95$

Figure 14: PSD plots for the clean cavity L/D 7 with doors comparing results from DES, SAS and URANS methods. Plots are for the front (a), middle (b) and rear (c) transducers on the cavity floor and presented in terms of SPL. CC - Clean Cavity, S-A - Spalart Allmaras.

OASPL plots for the doors on cases for L/D 5 and L/D 7 cavities are shown in Fig. 15 comparing DES, SAS and URANS methods with experimental data for the M219 cavity with doors on. For the L/D 5 cavity (Fig. 15(a)), DES, SAS and URANS captured the characteristic 'W' shape of the experimental data. DES and SAS showed an almost constant overprediction of 4dB while for URANS the maximum overprediction was 6dB. In the case of the L/D 7 cavity (Fig. 15(b)), DES and SAS showed similar shapes and magnitudes while URANS was underpredicted along the length of the cavity. Here, the 'W' shape is not as pronounced as in the L/D 5 case. The URANS did not predict the 'W' shape and as a result the magnitudes in the range of $x/L = 0.2$ to $x/L = 0.6$ are almost 5dB lower than the DES and SAS.

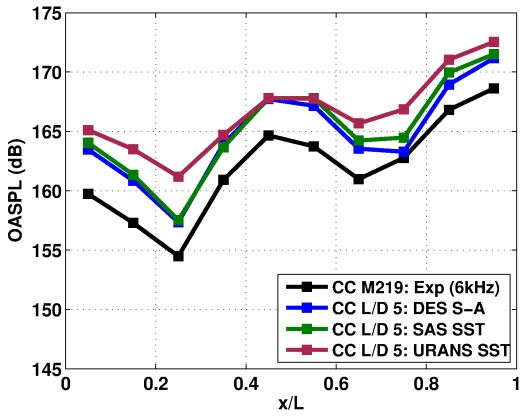

(a) Clean Cavity L/D 5

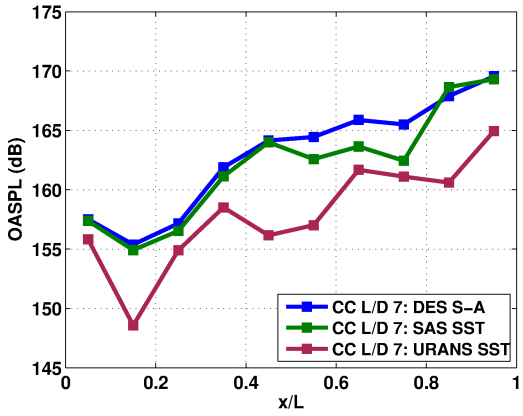

(b) Clean Cavity L/D 7

Figure 15: OASPL along the cavity floor for the clean cavity L/D 5 and 7 with doors. . For the L/D 5 cavity, plots are also compared to experimental data from Nightingale *et al.*[12].

The BISPL plots for the L/D 5 cavity with doors on in Fig. 16 show that the four modes are reasonably captured by both DES and SAS. The overprediction in the first mode for DES and SAS are between 1 to 4dB. For the dominant second mode, SAS is very similar in shape and magnitude to the experiment with an underprediction at two locations in the middle of the cavity of about 5dB. URANS captured the overall shapes of the first two modes and showed an overprediction for the last two modes along the first half of the cavity length. For the L/D 7 cavity (Fig.

17), URANS underpredicted the first, second and fourth modes compared to DES and SAS while mode three had a similar shape and magnitude. DES and SAS showed similar shapes and magnitudes for mode one and mode two with differences in mode three and mode four occurring around the middle of the cavity. A summary of the computational details of the different cavity configurations are given in Table 2. The clock time shown in hours is based on the use of 32 cores for each computational case.

Table 2 Summary of computational details of CFD calculations. CC: Clean Cavity. $S-A$: Spalart Allmaras.

Computation	Method	Clock Time (hr)
CC, L/D 5, Doors off	DES S-A	3909
	SAS k-ω	312
CC, L/D 5, Doors on	DES S-A	4560
	SAS k-ω	364
CC, L/D 7, Doors off	DES S-A	4100
	SAS k-ω	400
CC, L/D 7, Doors on	DES S-A	4850
	SAS k-ω	470

5.4 Joint Time-Frequency Analysis

The unsteadiness within the cavity was investigated using Joint Time-Frequency Analysis (JTFA) through Short-Time Fourier Transform (STFT)[33]. A space-time map of the dominant Rossiter modes on the cavity floor, for the L/D 5 cavity with doors off, was produced comparing the experimental data (Fig. 18(a)), DES (Fig. 18(b)) and SAS (Fig. 18(c)) results. Like in the experiment, mode two is seen to dominate along the middle of the cavity for DES and SAS with occasional mode switching to mode one and mode four. Along the front and rear end of the cavity, modes are seen to switch between one to three over time. The DES results show good comparison to the experiment where large regions of mode three are present at the front of the cavity and a mix of mode one, two and three are present at the rear. Mode three is seen to be intermittent at the front and rear of the cavity, for DES and more in SAS, compared to the experiment. The relatively low mode three in SAS and the high mode one suggests a shift of energy to lower frequency modes.

Similar plots were produced for the L/D 5 cavity with doors on comparing experimental data (Fig. 19(a)) and SAS (Fig. 19(b)) results. Here the effect of the doors is clearly by the dominance of the second mode along the length of the cavity with some mode one content towards the rear of the cavity. SAS is seen to produce similar frequency content as in the experiment but with relatively more mode three at the front and less of mode one at the back.

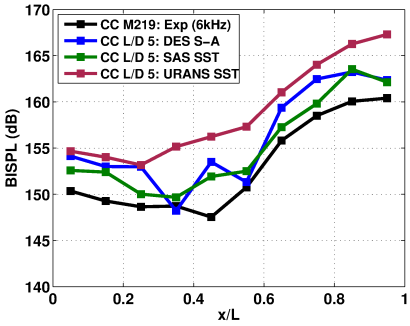

(a) Mode 1: $50 \leq f \leq 250$ Hz

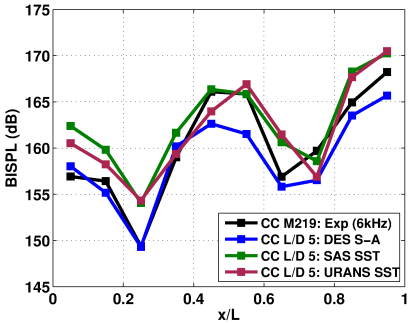

(b) Mode 2: $250 \leq f \leq 450$ Hz

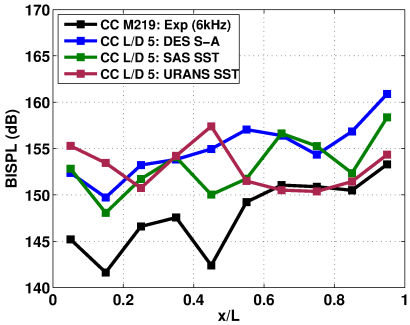

(c) Mode 3: $500 \leq f \leq 700$ Hz

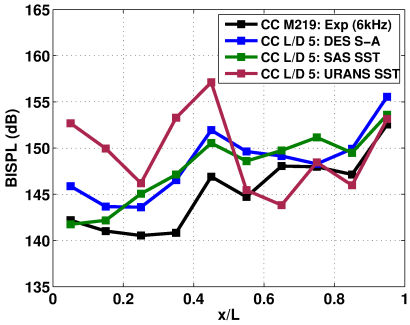

(d) Mode 4: $700 \leq f \leq 900$ Hz

Figure 16: BISPL along the cavity floor for the clean cavity L/D 5 with doors. Plots compare results from DES, SAS and URANS methods to experimental data from Nightingale *et al.*[12].

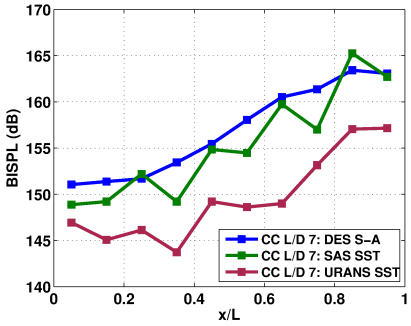

(a) Mode 1: $50 \leq f \leq 250$ Hz

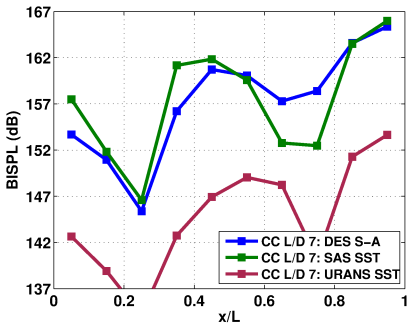

(b) Mode 2: $250 \leq f \leq 450$ Hz

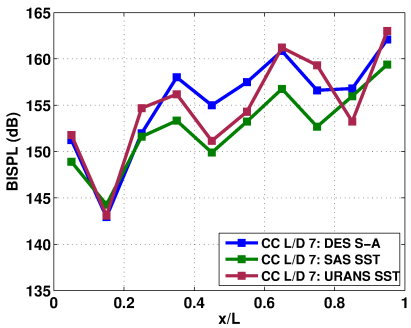

(c) Mode 3: $500 \leq f \leq 700$ Hz

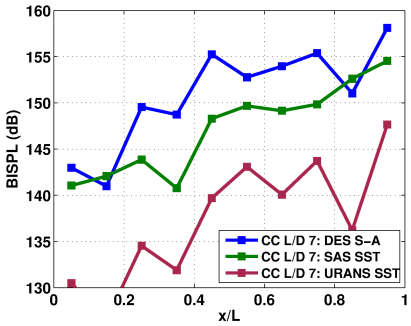

(d) Mode 4: $700 \leq f \leq 900$ Hz

Figure 17: BISPL along the cavity floor for the clean cavity L/D 7 with doors. Plots compare results from DES, SAS and URANS methods.

5.5 Proper Orthogonal Decomposition Analysis

To construct the POD modes, 101 snapshots were taken at regular intervals for the SAS computation of the

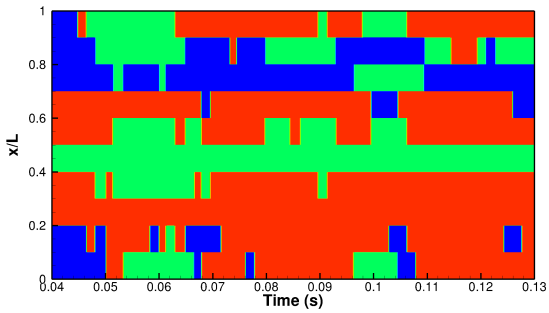

(a) Experiment

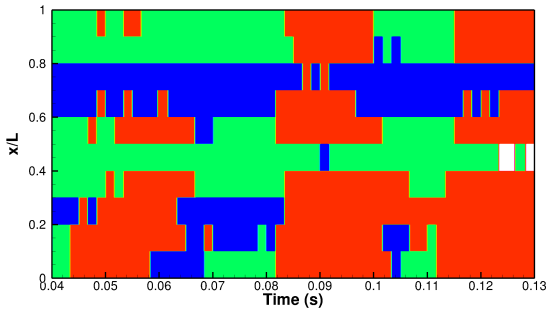

(b) DES

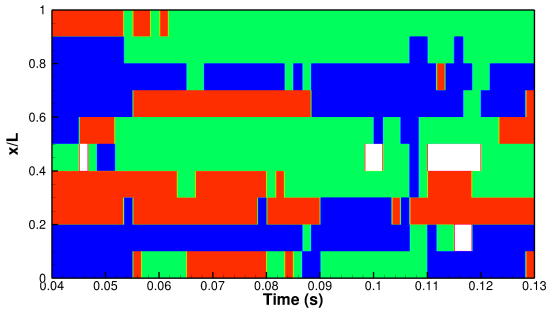

(c) SAS

Figure 18: Space–time maps along the floor for the clean cavity, L/D 5, without doors comparing results from DES (b) and SAS (c) to the experimental data (a) from Nightingale *et al.*[12]. The different colours represent: blue - mode 1, green - mode 2, red - mode 3, white - mode 4.

L/D 7 cavity with doors off. The POD was performed on the five primitive variables: density, u, v and w velocities and pressure. The three-dimensional cavity flow-field was reconstructed using 2, 11, 51 and 101 modes. This selection was limited by the available disk storage, for which the 101 snap-shots approached 100 GB for a mesh size of five million cells. With the mean mode ignored, the cumulative energy is shown in Fig. 20 for DES and SAS showing that pressure and density modes contained more energy than the velocity variables. As an example, the cumulative energy per mode from DES shows that 80% of the energy in pressure can be gained from 20 modes, whereas approximately 50 modes would be needed to gain the same value for the w velocity. This meant that the pressure field was more coherent and organised, and could be described using

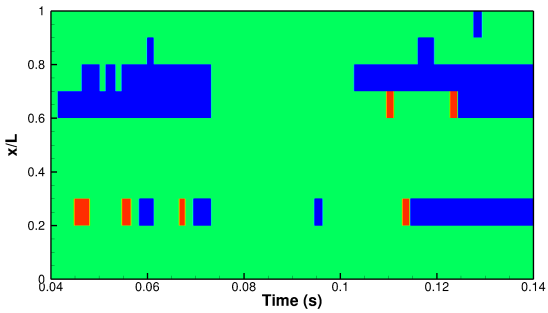

(a) Experiment

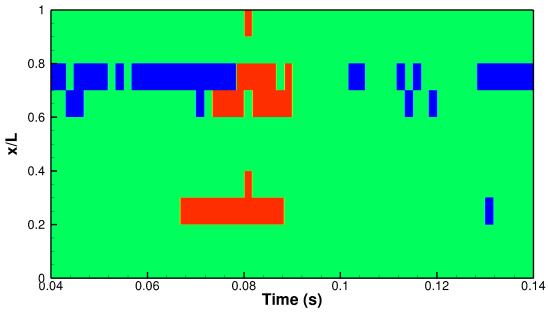

(b) SAS

Figure 19: Space–time maps along the floor for the clean cavity, L/D 5, with doors comparing results from SAS (b) to the experimental data (a) from Nightingale *et al.*[12]. The different colours represent: blue - mode 1, green - mode 2, red - mode 3, white - mode 4.

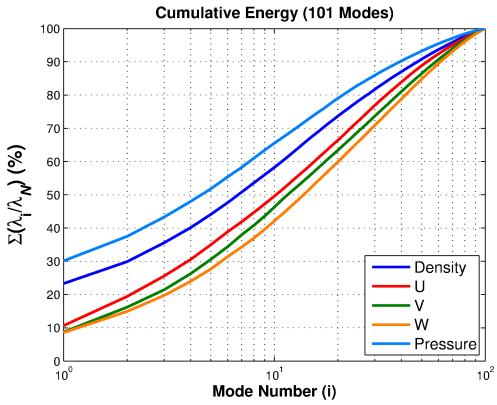

(a) DES

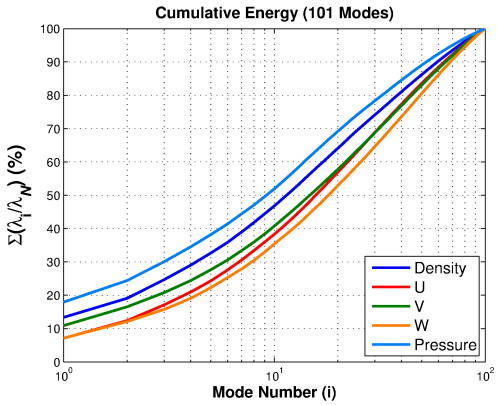

(b) SAS

Figure 20: Cumulative energy for increasing number of modes for DES (a) and SAS (b) results for the clean cavity L/D 7.

fewer modes, while the velocity fields contained smaller and possibly more turbulent structures, meaning that the energy was redistributed to the higher modes. For the modes constructed from SAS, the energy in the velocity variables per mode were similar to DES, however, the pressure and density variables showed a 10% decrease in the energy per mode. This means that while 80% of the energy in density can be gained from 20 modes of a DES solution, 30 modes are required from the SAS solution to gain the same amount of energy

The decomposition using 101 snapshots and a reduced set of 51 snapshots are compared in Fig. 21 for DES and SAS. The ratios of the modes to the first mode were quite similar for both decompositions (51 and 101) up to about mode number 20 for DES and SAS implying that even the reduced set would give a good indication of the structure of the flow, although the modes would not be as well resolved. The comparison of the decomposition between DES and SAS showed that most of the energy was contained within the lower modes. SAS shifted more of the energy into lower modes than DES. Pressure and normal velocity showed the biggest differences with curves for DES dropping faster after about 20 modes. This mean that more number of modes would be required by SAS to capture the lower levels of energy in the flow.

5.6 Flow-Field Reconstructions for Clean Cavity L/D 7

SAS flow-fields for the cavity L/D 7 without doors were reconstructed using 2, 11, 51 and 101 modes. The flow-fields from the reconstructions are shown in Fig. 22. Contours of Mach number at the cavity centreline show that the full dynamics of the shear layer was only represented when 51 modes or more were used. Structures inside the cavity only began to appear when 51 modes were used.

The areas of high difference were generally restricted to the aft half of the cavity. Reconstructions from 51 modes gave significant improvement, although differences still appeared in areas around the aft wall and shear layer where the smallest structures occurred. It should be noted that the time-varying mean flow-field (POD mode 1) was always included in the reconstructions. Therefore when the reconstructed data are averaged, the flow-field was unaffected by the number of modes used in the reconstruction.

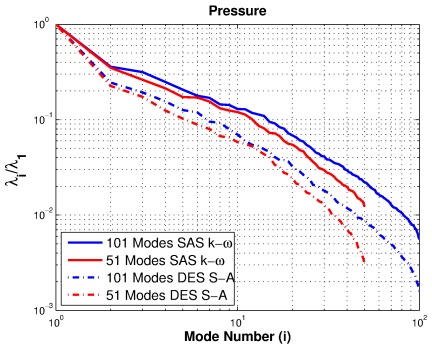

(a) Pressure

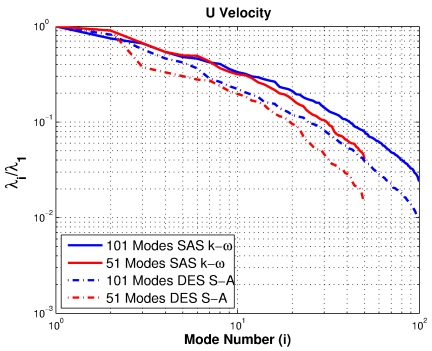

(b) Streamwise Velocity

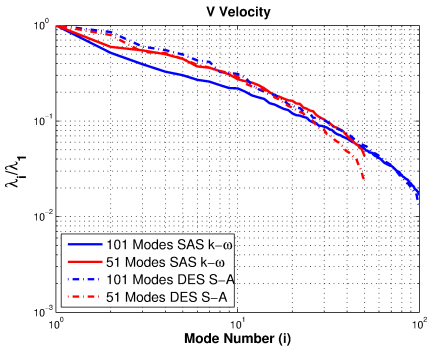

(c) Normal Velocity

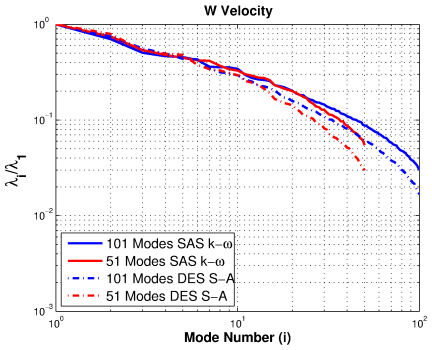

(d) Spanwise Velocity

Figure 21: Mode eigenvalues normalised by the first mode eigenvalue comparing the POD for DES (a) and SAS (b) results for the clean cavity L/D 7 comparing DES and SAS results for reduced sets of 51 and 101 modes.

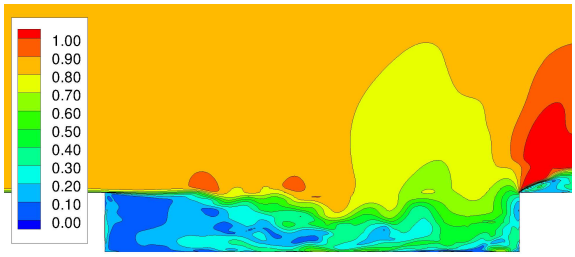

(a) Original

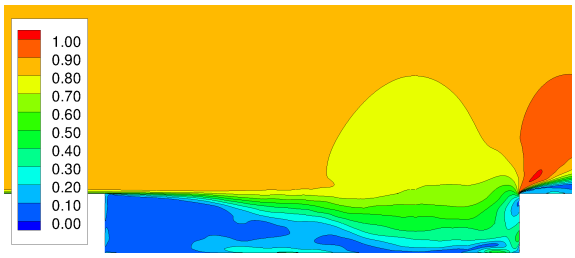

(b) 2 Modes

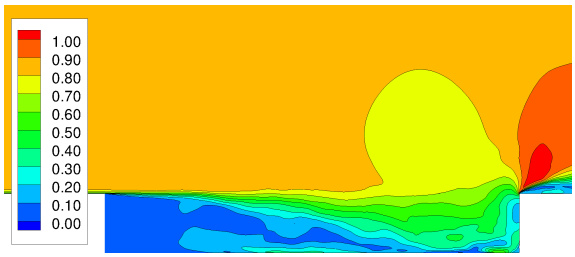

(c) 11 Modes

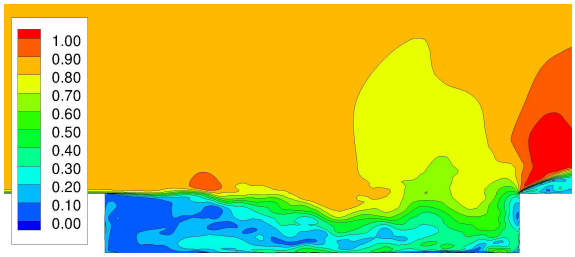

(d) 51 Modes

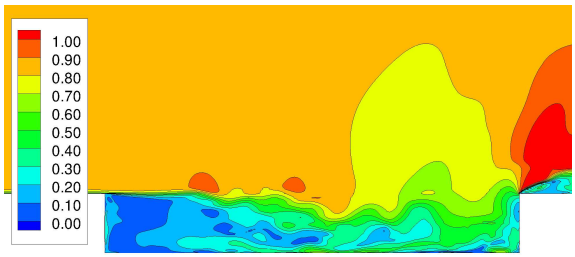

(e) 101 Modes

Figure 22: Reconstruction of the SAS computation for the L/D 7 cavity Mach field using increasing number of modes. Contours are shown at the cavity centreline and range from 0 (blue) to 1 (red).

6 Summary and Conclusions

Simulations for the flow over transonic cavities were carried out for cavities of L/D 5 and 7 with and without doors. Flow visualisations showed the unsteadiness and

breakdown of the shear layer, the upstream propagation of acoustic waves from the aft wall and away from the cavities. Q-Criteria revealed the structures present inside and along the length of the cavities. Results from DES, SAS and URANS were compared with experimental results for the L/D 5 case and revealed fundamental differences between the two configurations. Unsteady pressure data along the floor that revealed the spectra for the cavities with doors off were dominated by multiple peaks from the first, second and third modes, however, the cavities with doors on were dominated by the second mode only. The dominant modes of the cavity shifted between the L/D 5 and L/D 7 case with doors off where modes two and three were dominant for L/D 5 and modes one and two were dominant for L/D 7. The addition of the doors stopped this shifting of modes and retained dominance of the second mode for both types of cavities with the L/D 7 being quieter than the L/D 5 by 10dB. The JTFA showed the mode switching nature of the L/D 5 cavity without doors and also highlighted the dominance of the second mode along the middle of the cavity. SAS produced results at about a 10th of the time of DES and showed good agreement with experimental results for the L/D 5 cavity and good agreement with the DES results for the L/D 7 cavity for which experimental results were not available. The use of POD to reduce the information stored demonstrated that approximately 85% of the flow energy needed to be retained for an accurate flowfield reconstruction. Future work will focus on simulations of a store in the cavity to further demonstrate the use of SAS and the possibility to extend it to the problem of store release from cavities.

Acknowledgements

The financial support of the Engineering and Physical Sciences Research Council and MBDA through Industrial CASE: 09000510 is gratefully acknowledged. The authors would also like to thank Nigel Taylor of MBDA for his support in this work. The use of the POLARIS HPC cluster of N8 and the Chadwick HPC cluster of the University of Liverpool are also gratefully acknowledged. A. Kusyumov is supported by a grant according to the decree no. 200 of the Russian Federation Government about Attracting Leading Scientists to Russian Educational Institutions (agreement No 11.G34.31.0038).

References and Notes

1 M. Murayama, Y. Yokokawa and K. Yamamoto, *Computational Study On Noise Generation From A Two-Wheel Main Landing Gear*, Aviation Program Group, Japan Aerospace Exploration Agency, ICAS, 2012.

2 N. Molin, J.F. Piet, L.C. Chow, M.G. Smith, W.M. Dobrzynski and C. Seror, Prediction of Low Noise Aircraft Landing Gears and Comparison with Test Results, AIAA 2006-2623, 2006.

3 W.H. Herkes, R.F. Olsen and S. Uellenberg, The Quiet Technology Demonstrator Program: Flight Validation of Airplane Noise-Reduction Concepts, AIAA 2006-2720, 2006.

4 R. Elkoby, L. Brusniak, R. Stoker, M.R. Khorrami, A. Abeysinghe and J. Moe, Airframe Noise Test Results from the QTD II Flight Test Program, AIAA 2007-3457, 2007.

5 S.J. Lawson and G.N. Barakos, Evaluation of DES for Weapons Bays in UCAVs, Aerospace Science and Technology, In Press, doi:10.1016/j.ast.2010.04.006, 2010.

6 F.R. Menter, M. Kuntz and R. Bender, A Scale-Adaptive Simulation Model for Turbulent Flow Predictions, 41st Aerospace Sciences Meeting and Exhibit, DOI: 10.2514/6.2003-767, 06 - 09 January, 2003.

7 F.R. Menter and Y. Egorov. Revisiting The Turbulent Length Scale Equation. In IUTAM Symposium: One Hundred Years of Boundary Layer Research, Gottingen, 2004.

8 F.R. Menter and Y. Egorov. A Scale-Adaptive Simulation Model Using Two-Equation Models. AIAA paper 20051095, Reno, NV, 2005.

9 F.R Menter, Y. Egorov, The Scale-Adaptive Simulation Method for Unsteady Turbulent Flow Predictions. Part 1: Theory and Model Description, Flow Turbulence Combustion, Vol. 85, pp. 113138, 2010.

10 Y. Egorov, F. Menter, R. Lechner and D. Cokljat, The Scale-Adaptive Simulation Method for Unsteady Turbulent Flow Predictions. Part 2: Application to Complex Flows, Flow Turbulence Combustion, Vol. 85, pp. 139165, 2010.

11 G.N. Barakos, R. Steijl, K. Badcock, and A. Brocklehurst, Development of CFD capability for full helicopter engineering analysis, 31st European Rotorcraft Forum, v. 2005, p. 91.1-91.15, 2005.

12 D.A. Nightingale, J.A. Ross and G.W. Foster, Cavity Unsteady Pressure Measurements - Examples from Wind-Tunnel Tests, Technical Report Version 3, Aerodynamics & Aeromechanics Systems Group, QinetiQ, November, 2005.

13 P.R. Spalart and S.R. Allmaras, A One-Equation Turbulence Model for Aerodynamic Flows, La Recherche Aerospatiale, 1, 5-1, 1994.

14 G.N. Barakos, S.J. Lawson, R. Steijl, and P. Nayyar, Numerical Simulations of High Speed Turbulent Cavity Flows, Flow, Turbulence and Combustion, 83(4):569585, December, 2009.

15 S. Osher and S. Chakravarthy, Upwind Schemes and Boundary Conditions with Applications to Euler Equations in General Geometries. Journal of Computational Physics, Volume 50, Issue 3, p. 447-481, DOI: 10.1016/0021-9991(83)90106-7, 1983

16 P.L Roe, Approximate Riemann Solvers, Parameter Vectors, and Difference Schemes.Journal of Computational Physics, Volume 43, Issue 2, October 1981, Pages 357372.

17 B. van Leer, Towards the ultimate conservative difference scheme. V. A second-order sequel to Godunov's method. Journal of Computational Physics, Volume 32, Issue 1, July 1979, Pages 101136.

18 G.D. van Albada, B. van Leer, W.W. Roberts, A Comparative Study of Computational Methods in Cosmic Gas Dynamics. Astronomy and Astrophysics, Volume 108, No. 1, April 1982, Pages 76-84.

19 A. Jameson, Time Dependent Calculations Using Multigrid, with Applications to Unsteady Flows Past Airfoils and Wings, AIAA Paper 91-1596, AIAA 10th Computational Fluid Dynamics Conference, Honolulu, June 1991.

20 O. Axelsson, Iterative Solution Methods. Cambridge University Press: New Ed edition, 29 March 1996.

21 F.R. Menter, Two-Equation Eddy-Viscosity Turbulence Models for Engineering Applications, AIAA Journal, Vol. 32, No. 8, August 1994, pp. 1598-1605.

22 D.G. Childers (ed.), Modern Spectrum Analysis. chap. 2, pp. 23148. IEEE Press, New York, 1978.

23 L. Larcheveque, P. Sagaut, T.-H Le, and P. Comte, Large-Eddy Simulation of a Compressible Flow in a Three-Dimensional Open Cavity at High Reynolds Number, Journal of Fluid Mechanics, 516:265301, 2004.

24 A.D. Pierce, Acoustics: An Introduction to its Physical Principles and Applications. Woodbury, New York: Acoustical Society of America, 1989.

25 J.E. Rossiter, Wind Tunnel Experiments on the Flow Over Rectangular Cavities at Subsonic and Transonic Speeds, Technical Report 64037, Royal Aircraft Establishment, October, 1964.

26 H.H. Heller, D.G. Holmes. and Covert, E., Flow Induced Pressure Oscillations in Shallow Cavities, Journal of Sound and Vibration, Vol. 18(4), pp. 545-553, October, 1971.

27 J.C.R Hunt, A.A. Wray, and P. Moin, Eddies, Streams and Convergence Zones in Turbulent Flows, In Proceedings of the Summer Program, Center for Turbulence Research, pages 193207, N89-24555, 1988.

28 J. Jeong and F. Hussain, On the Identification of a Vortex, Journal of Fluid Mechanics, 285:6994, 1995.

29 G. Berkooz, P. Holmes and J.L. Lumley, The Proper Orthogonal Decomposition in the Analysis of Turbulent Flows, Annual Review of Fluid Mechanics, 25:539 575, 1993.

30 J.L. Lumley, Stochastic Tools in Turbulence, Volume 12 of Applied Mathematics and Mechanics, An International Series of Monographs. Academic Press, 1970.

31 ANSYS Inc, ICEM CFD v13 - User Manual. (Available from: http://www.academia.edu/3196257/ANSYS_ICEM_CFD_13_-_User_Manual)[Accessed on 28th March 2014].

32 J.A. Ross, Cavity Acoustic Measurements At High Speeds.Technical Report DERA/MSS/MSFC2/ TR000173, QinetiQ, March, 2000.

33 J.B. Allen, Short Time Spectral Analysis, Synthesis, and Modification by Discrete Fourier Transform. IEEE Transactions on Acoustics, Speech, and Signal Processing. ASSP-25 (3): 235238, June 1977.